

# Numerical Investigation of the Unsteady Flow Past an Iced Multi-Element Airfoil

Maochao Xiao\* and Yufei Zhang†

*Tsinghua University, 100084 Beijing, People's Republic of China*

and

Feng Zhou‡

*Shanghai Aircraft Design and Research Institute, 201210 Shanghai, People's Republic of China*

<https://doi.org/10.2514/1.J059114>

Unsteady flow characteristics are investigated using wall-modeled large-eddy simulation for a 30P30N three-element airfoil with streamwise ice and horn ice accreted at its slat leading edge, respectively. The ice accretions cause massive flow separation above the slat, which results in a surface pressure plateau on the slat and further unloads the downstream wing elements. The above mentioned two ice shapes lead to lift decreases of 10.66 and 16.45% and drag increases of 44.58 and 59.42%, respectively. Ice-induced vortices first roll up due to Kelvin–Helmholtz instability above the slat with ice accretions, and the subsequent vortex pairing halves their characteristic motion frequency. The developed vortices, composed of multiscale structures, dominate the slat upper surface and are convected through the main element to aggravate the flow separation over the flap. Moreover, extremely strong acoustic resonance occurs in the iced slat cove, and its tonal frequencies are consistent with theoretical model predictions. These intense tones are believed to result from the elevated pressure fluctuations along the cavity free shear layer, which are in turn related to the propagation of the ice-induced pressure fluctuations from above the slat because their most dominant frequencies identified by proper orthogonal decomposition are nearly equal to the resonant frequencies.

## Nomenclature

$AoA$	=	angle of attack
$C_D$	=	drag coefficient
$C_L$	=	lift coefficient
$C_p$	=	pressure coefficient
$c$	=	airfoil chord length
$f$	=	frequency
$Ma$	=	Mach number
$P_\infty$	=	freestream pressure
$Q$	=	second invariant of the velocity gradient tensor
$Re$	=	Reynolds number
$U$	=	time-averaged velocity
$U_\infty$	=	freestream velocity
$u, v, w$	=	instantaneous velocity
$x, y$	=	Cartesian coordinates
$\Omega_\tau$	=	spanwise vorticity
$\langle \rangle$	=	averaged flow quantity

## I. Introduction

ICE accretions on an aircraft lifting surface can lead to substantial reductions in maximum lift, control surface effectiveness, and stall angle of attack (AoA), and a noticeable increase in drag [1].

Received 3 October 2019; revision received 24 March 2020; accepted for publication 30 March 2020; published online 22 May 2020. Copyright © 2020 by Maochao Xiao, Yufei Zhang, and Feng Zhou. Published by the American Institute of Aeronautics and Astronautics, Inc., with permission. All requests for copying and permission to reprint should be submitted to CCC at [www.copyright.com](http://www.copyright.com); employ the eISSN 1533-385X to initiate your request. See also AIAA Rights and Permissions [www.aiaa.org/randp](http://www.aiaa.org/randp).

\*Graduate Student, School of Aerospace Engineering; also Key Laboratory of Icing and Anti/De-icing, China Aerodynamics Research and Development Center, 621000 Mianyang Sichuan, People's Republic of China. Student Member AIAA.

†Associate Professor, School of Aerospace Engineering; also Key Laboratory of Icing and Anti/De-icing, China Aerodynamics Research and Development Center, 621000 Mianyang Sichuan, People's Republic of China; [zhangyufei@tsinghua.edu.cn](mailto:zhangyufei@tsinghua.edu.cn). Senior Member AIAA (Corresponding Author).

‡Senior Engineer.

Although aircraft icing has been studied for a long period, it is still a contributing factor in approximately 10% of all weather-related accidents among general aviation aircrafts [2].

Ice accretions on an aircraft are classified into four categories based on their geometry: roughness, streamwise ice, horn ice, and spanwise-ridge ice [3]. Of these, the horn and spanwise-ridge ice shapes cause strong disturbance to a flowfield. Many studies [4–7] have investigated icing effects on airfoil aerodynamics. The leading-edge horn-ice-accreted airfoil is of particular concern because the flow past the iced airfoil is dominated by a separation bubble aft of the ice, which causes a surface pressure plateau and induces a thin-airfoil stall type. Ansell and Bragg [8] and Manshadi and Esfeh [9] identified two dominant frequencies caused by horn-ice-induced unsteadiness for an airfoil: a regular vortical motion frequency near or downstream of the reattachment and a separated-shear-layer flapping frequency corresponding to the quasi-periodic deforming of the ice-induced separation bubble. Moreover, a thin-airfoil stall frequency exists due to the circulation oscillation around an airfoil [10].

The systematic assessment of icing effects on a multi-element airfoil is more complicated than that on a single-element airfoil due to the complex flow physics; this partly accounts for the small number of relevant investigations hitherto [1]. Ingelman-Sundberg et al. [11] reported a maximum penalty of 20% in lift and a reduction of 6 deg in stall AoA due to ice accretion for a NACA 65A215 airfoil with a vane flap. In contrast with a main element or flap, ice accretions on a slat not only cause more dramatic variations in lift and drag but also lead to a noticeable reduction in stall AoA [12]. Furthermore, the ice shapes accreted on the slat upper surface tend to bring about a lift curve with a flatter top [13].

Numerical simulation plays an important role in aerodynamic investigations. The Reynolds-averaged Navier–Stokes (RANS) method has been widely applied in industrial simulations. However, RANS models demonstrate severe drawbacks for predicting ice-induced separated flows [14]. They tend to overpredict the upper-surface plateau pressure and underpredict the maximum lift and stall AoA for an airfoil with a leading-edge ice horn [15,16].

Hybrid RANS–large-eddy simulation (RANS–LES) methods show superiority in predicting massively separated flows under high-Reynolds-number conditions. It typically achieves a higher accuracy than RANS and involves a more acceptable cost than large-eddy simulation (LES). Pan and Loth [2] reported that detached-eddy

simulation (DES), which is a kind of hybrid RANS-LES method, predicts a more consistent stall behavior with experiments than the RANS method does, although the lift deviations between the DES-predicted values and the experimental data are still considerable. Choo et al. [17] indicated that DES predicts more extensive flow separation bubbles than the experimental measurements for the GLC 305 airfoil with a 944 ice horn. Alam et al. [18] and Xiao et al. [19] attributed the overestimation of separation bubbles by DES to the predicted delayed Kelvin–Helmholtz (K-H) instability of the ice-induced separated shear layer (SSL). Alam et al. [18] employed a dynamic hybrid RANS-LES method, and Xiao et al. [19] applied a low-dissipation numerical scheme to accelerate K-H instability. Some improvements based on the zonal DES method have also been reported [20,21]. Recently, the present authors [22] have shown the superiority of a wall-modeled LES (WMLES) in predicting ice-induced flow separation and especially in resolving the roll-up of vortices induced by K-H instability.

Although there have been some numerical investigations of icing effects on single-element iced airfoils, numerical research on multi-element airfoils is lacking. In this paper, a WMLES method is adopted to study the separated flow of a 30P30N three-element airfoil with its slat accreted with horn ice and streamwise ice, respectively. To the best of the authors' knowledge, this is the first LES investigation of the unsteady flow characteristics of an iced multi-element airfoil. The computational method is first validated by two cases. Then, the numerical results for the iced 30P30N airfoil are analyzed with a highlight on the turbulent structures.

## II. Methods of Computation and Analysis

### A. WMLES Method

The filtered Navier–Stokes equations are solved using an in-house-structured finite-volume CFD code [23,24]. The time integration is discretized using a third-order Runge–Kutta method. The viscous term is discretized by a second-order central difference scheme. The inviscid flux is computed through the blending of a dissipative upwind scheme and a nondissipative central difference scheme:

$$F = (1 - \sigma)F^{\text{central}} + \sigma F^{\text{upwind}} \quad (1)$$

where  $0 \leq \sigma \leq 1$  is a blending parameter. The blending parameter  $\sigma$  is computed based on grid point coordinates, as in [25]:

$$\sigma = c \|D + D^T\| \quad (2)$$

where  $c = 2$  is a constant and  $D$  is a differencing operator. On a uniform Cartesian grid, a skew-symmetric operator ( $D^T = -D$ ) is obtained when a polynomial reconstruction is employed to calculate the left- and right-biased states of a control volume face, whereas on a nonuniform/irregular grid, a non-skew-symmetric differencing operator ( $D^T \neq -D$ ) is obtained. Consequently, the blending parameter  $\sigma$  is zero in the regions with a perfect grid to decrease numerical dissipation; it is nonzero in the regions with a less-than-perfect grid to add numerical dissipation and stabilize the solution. The numerical method for calculating  $\sigma$  was originally developed for an unstructured solver [25]. Here, it is applied to a structured code [22]. In Eq. (1), the central flux is discretized via a second-order central difference scheme, and the upwind flux is computed using Roe's scheme [26] coupled with fifth-order weighted essentially nonoscillatory interpolation [27].

Vreman's eddy viscosity model [28] is adopted to model subgrid-scale turbulent motions. An equilibrium stress-balanced wall model is adopted to model the energy-containing eddies in the inner turbulent boundary layer [29]:

$$\frac{\partial}{\partial y} \left[ (\mu + \mu_t) \frac{\partial u}{\partial y} \right] = 0 \quad (3)$$

$$\frac{\partial}{\partial y} \left[ (\mu + \mu_t) u \frac{\partial u}{\partial y} + c_p \left( \frac{\mu}{Pr} + \frac{\mu_t}{Pr_t} \right) \frac{\partial T}{\partial y} \right] = 0 \quad (4)$$

where  $\mu$  and  $\mu_t$  are the laminar and turbulent viscosities, respectively;  $Pr = 0.72$  and  $Pr_t = 0.90$  are the laminar and turbulent Prandtl numbers, respectively;  $c_p$  is the specific heat at constant pressure;  $u$  is the wall-parallel velocity; and  $T$  is the temperature. The eddy viscosity  $\mu_t$  is computed by a mixing-length model  $\mu_t/\mu = \kappa y^+ [1 - \exp(-y^+/A^+)]^2$ , where  $A^+ = 17$  and the Karman constant  $\kappa = 0.41$ .

Equations (3) and (4) are solved on an embedded (overlapping) unidimensional grid near the wall with 50 points in the wall-normal direction and with  $\Delta y^+ < 1$  for the first off-wall point. In the present study, the wall model covers 2.5 layers of LES grid cells in the wall-normal direction, as suggested by Kawai and Larsson [29], extending to the logarithmic layer. The boundary conditions at the wall are adiabatic no-slip conditions. The information at the top boundary is directly taken from the computed LES flow at the cell center of the third off-wall cell layer. The wall shear stress  $\tau_w = \partial u / \partial y|_{\text{wall}}$  and wall heat flux  $q_w = k \partial T / \partial y|_{\text{wall}}$  yielded from Eqs. (3) and (4) are applied as the wall boundary conditions of the LES computation.

### B. POD Method

The application of proper orthogonal decomposition (POD) to identify dominating flow structures dates back to Lumley's work [30] on atmospheric flows. Since then, the method has been widely used to study various flows, such as free shear layers [31], jets [32], and separation bubbles [33]. The POD decomposes a flowfield into a series of spatial modes such that

$$\mathbf{u}'(\mathbf{x}, t_k) = \sum_{n=1}^{N_{\text{mode}}} \alpha^n(t_k) \cdot \boldsymbol{\varphi}^n(\mathbf{x}) \quad (5)$$

where  $\mathbf{u}'(\mathbf{x}, t_k)$  can be a fluctuating velocity or pressure field at a moment,  $\alpha^n(t_k)$  are the temporal coefficients,  $\boldsymbol{\varphi}^n(\mathbf{x})$  are the spatial modes, and  $N_{\text{mode}}$  is the number of POD modes applied for reconstruction. The snapshot POD method applied here [34] requires solving the eigenvalue problem

$$\mathbf{C} \alpha^n = \lambda^n \alpha^n \quad (6)$$

where  $\mathbf{C}$  is the positive symmetric covariance matrix with leading dimension  $N_{\text{snap}}$  (the number of snapshots). Its element  $C_{ij}$  is defined as the inner product of two snapshots:

$$C_{ij} = \frac{1}{N} (\mathbf{u}'(\mathbf{x}, t_i), \mathbf{u}'(\mathbf{x}, t_j))_{\Omega} \quad (7)$$

The positive real eigenvalues  $\lambda^n$ , which decrease monotonically with  $n$ , represent the relative energy of mode  $n$ . The temporal coefficients are the eigenvectors  $\alpha^n$ , and the spatial modes are obtained by

$$\boldsymbol{\varphi}^n(\mathbf{x}) = \frac{1}{N_{\text{snap}} \lambda^n} \sum_{k=1}^{N_{\text{snap}}} \alpha^n(t_k) \mathbf{u}'(\mathbf{x}, t_k) \quad (8)$$

The spatial modes, sorted by their relative energy, are orthogonal in space; the temporal coefficients are composed of multiple frequency components. A detailed introduction of the snapshot POD method can be found in [34].

## III. Validations

The WMLES method is validated through the flows around a clean 30P30N multi-element airfoil and an NLF-0414 airfoil with leading-edge horn ice shape 623. Figure 1 shows the computational geometries along with grids. For the 30P30N airfoil [35], the lengths of the slat and flap are  $0.15c$  and  $0.30c$ , respectively, and their deflection angles are both  $30^\circ$ . The trailing edges of both the slat and main

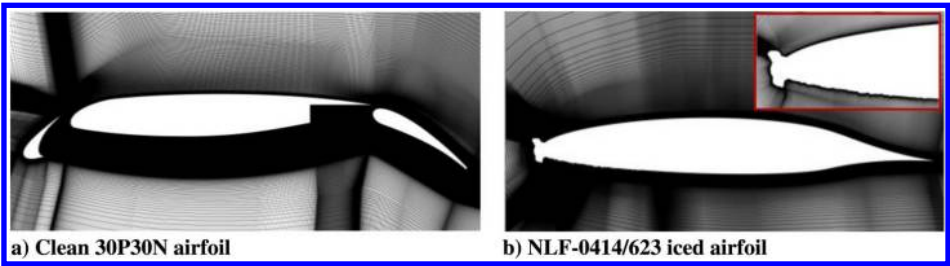


Fig. 1 Computational x-y plane geometries along with grids.

wing are sharp and that of the flap is thick. The spanwise length is taken as  $0.1c$  [36] and the freestream conditions are  $Ma = 0.17$ ,  $Re = 1.7 \times 10^6$ , and  $AoA = 5.5^\circ$ . For the NLF-0414/623 airfoil [7,37], an upper horn and a lower horn are accreted at the leading edge. Although three-dimensional (3D) ice accretion with spanwise variations was accreted in a real icing test, the ice shape used in the present study is two-dimensional (2D), which was captured from the tracing at a 30% spanwise location of the 3D ice accretion. For the 2D ice shape, experimental lift and surface pressure coefficients are provided in reference [7]; the lift coefficients were computed by surface pressure integration. In this computation, the spanwise size is set as  $0.2c$ , and the freestream condition is  $Ma = 0.21$  and

$Re = 4.6 \times 10^6$ . Three AoAs,  $3.0^\circ$ ,  $5.2^\circ$ , and  $7.0^\circ$  are computed. For both airfoils, the far-field boundary is located approximately  $50c$  away from the airfoil in both cases. Periodic boundary condition is applied in the spanwise direction, and the adiabatic no-slip boundary condition is set on the walls. The grid details for both configurations are listed in Table 1, where  $N_x$  and  $N_z$  are the respective cell numbers along the circumferential and spanwise directions and  $N_{total}$  is the total cell number.

Figure 2 illustrates the wall-parallel size  $\Delta x^+$  and wall-normal size  $\Delta y^+$  for the first off-wall grid cells. These results are obtained based on the skin friction provided by WMLES computations. For the clean 30P30N case, one can observe that  $\Delta x^+ < 200$  and  $\Delta y^+ < 30$  are met

Table 1 Grid details of the two configurations

Configuration	$N_{total}$ (million)	$N_x$	$N_{x,slat}$	$N_{x,Main}$	$N_{x,flap}$	$N_z$	First-layer height ( $\Delta y/c$ )	Time step ( $\Delta t U_\infty/c$ )
Clean 30P30N	30.8	2024	568	974	482	60	$2.5 \times 10^{-4}$	$2.0 \times 10^{-5}$
NLF-0414/623	31.8	1652	—	—	—	160	$1.5 \times 10^{-4}$	$1.7 \times 10^{-5}$

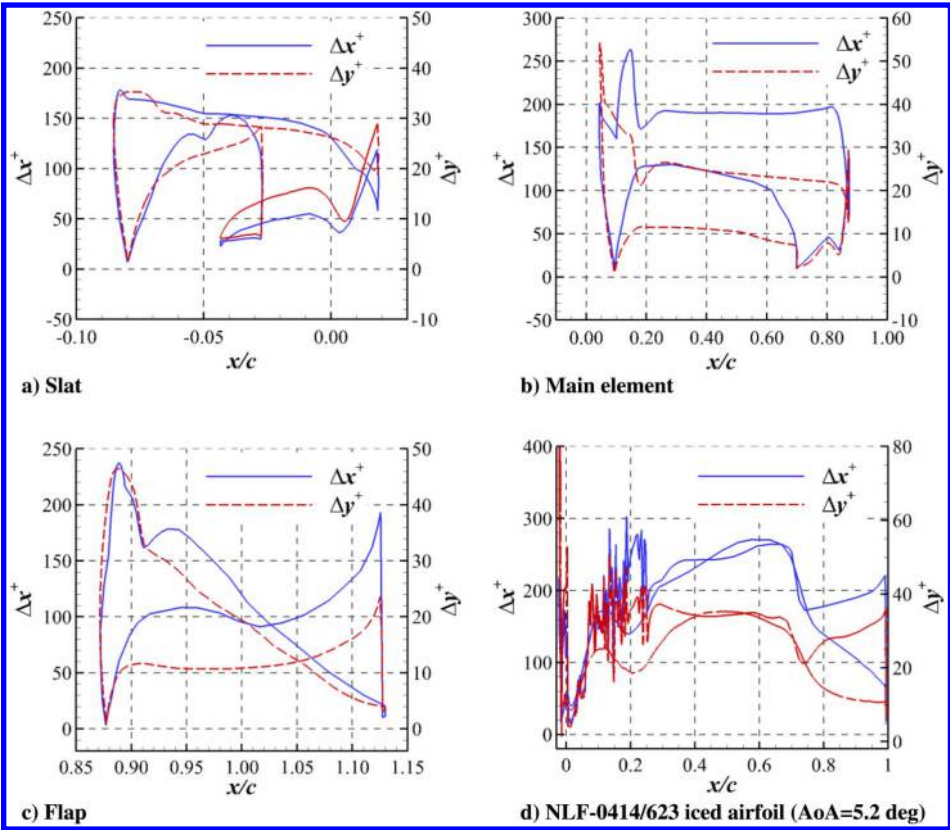


Fig. 2 Sizes of the first off-wall cells in wall units.

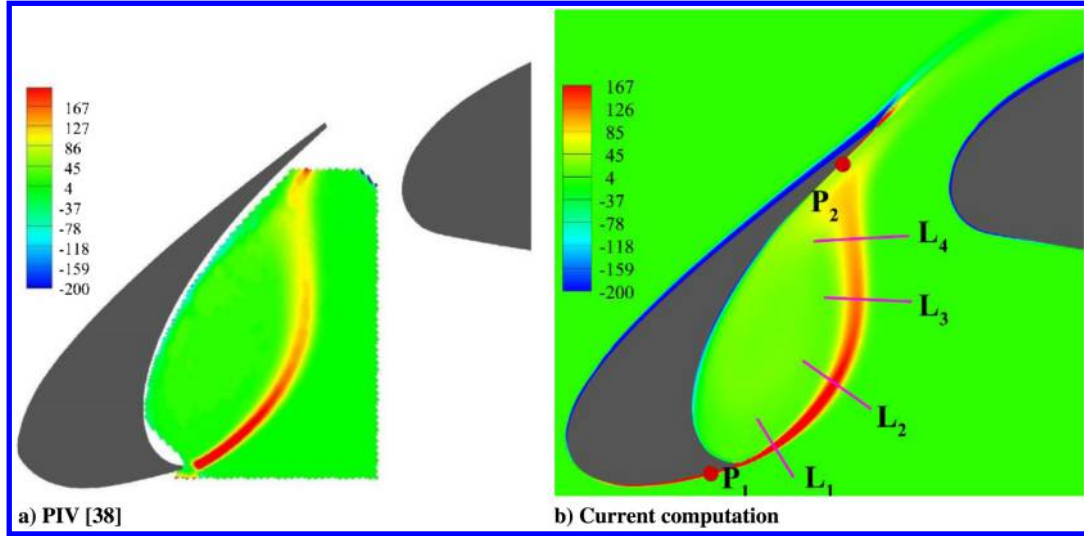


Fig. 3 Contours of mean spanwise vorticity  $\Omega_z(c/U_\infty)$  ( $Ma = 0.17$ ,  $Re = 1.7 \times 10^6$ ,  $AoA = 5.5^\circ$ ).

for most surface regions, except in the leading-edge area of both the main element and flap. Since  $\Delta z \approx 6.5\Delta y$ ,  $\Delta z^+ < 200$  is met for most surface regions. For the NLF-0414/623 iced airfoil,  $\Delta x^+ < 280$  and  $\Delta y^+ < 35$  are satisfied for most surface area, although they are larger at the leading edge of the upper horn and on some lower surface area with irregular ice accretions. In the spanwise direction,  $\Delta z$  is approximately 8–9 times the size of  $\Delta y$ .

#### A. Clean 30P30N Airfoil

Figure 3 compares the contours of the mean spanwise vorticity  $\Omega_z(c/U_\infty)$  obtained from PIV measurement [38] and from current computation. The two contours are highly consistent except for a predicted slightly thinner initial SSL, where the reliability of the experiment can be questionable because the region is near the corner of the PIV laser sheet. Besides, the computation yields slightly stronger vortical motions in the impingement region, where an accurate prediction can be challenging due to the interaction between the SSL and the boundary layer [39]. Figure 4 further compares the

velocity magnitude  $|U| = \sqrt{\langle u \rangle^2 + \langle v \rangle^2}$  with the experimental data [35] along the lines  $L_1$  to  $L_4$  (Fig. 3b) from left to right. The computed profiles fit well with the experimental data.

Figure 5 shows the power spectral density (PSD) of pressure fluctuations obtained by fast Fourier transform (FFT) at surface points  $P_1$  and  $P_2$  in Fig. 3b. At  $P_1$ , the low-frequency part of PSD agrees well with the experiments, and the high-frequency part agrees with the Japan Aerospace Exploration Agency (JAXA) data [40] but is slightly lower than that of the Florida State University (FSU) data [41]. The tonal peaks relevant to acoustic resonance inside the slat cove are well captured.  $P_2$  is located in the impingement region, where turbulent fluctuations are elevated. The predicted spectra are consistent with the experimental data.

#### B. NLF-0414/623 Iced Airfoil

Figures 6a and 6b compare the calculated lift and drag coefficients with the experimental results [7]. The RANS results are obtained

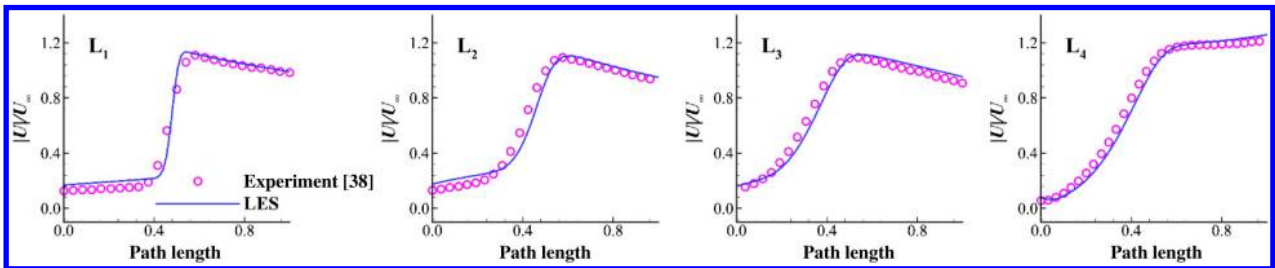


Fig. 4 Velocity magnitude  $|U|/U_\infty$  along  $L_1$ – $L_4$  in Fig. 3b ( $Ma = 0.17$ ,  $Re = 1.7 \times 10^6$ ,  $AoA = 5.5^\circ$ ).

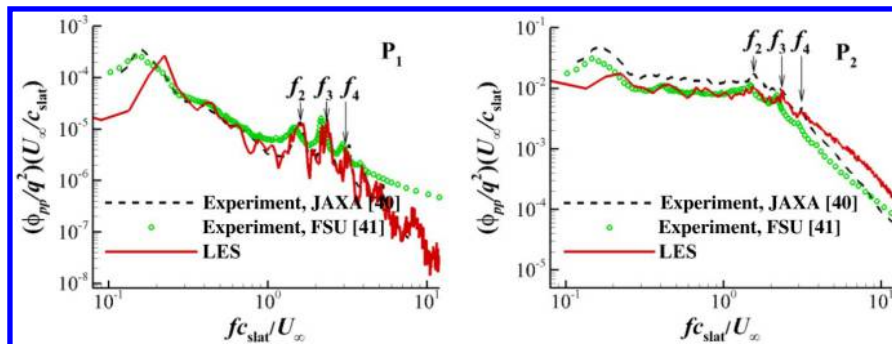


Fig. 5 PSD of pressure fluctuations at surface points  $P_1$  and  $P_2$  ( $Ma = 0.17$ ,  $Re = 1.7 \times 10^6$ ,  $AoA = 5.5^\circ$ ).



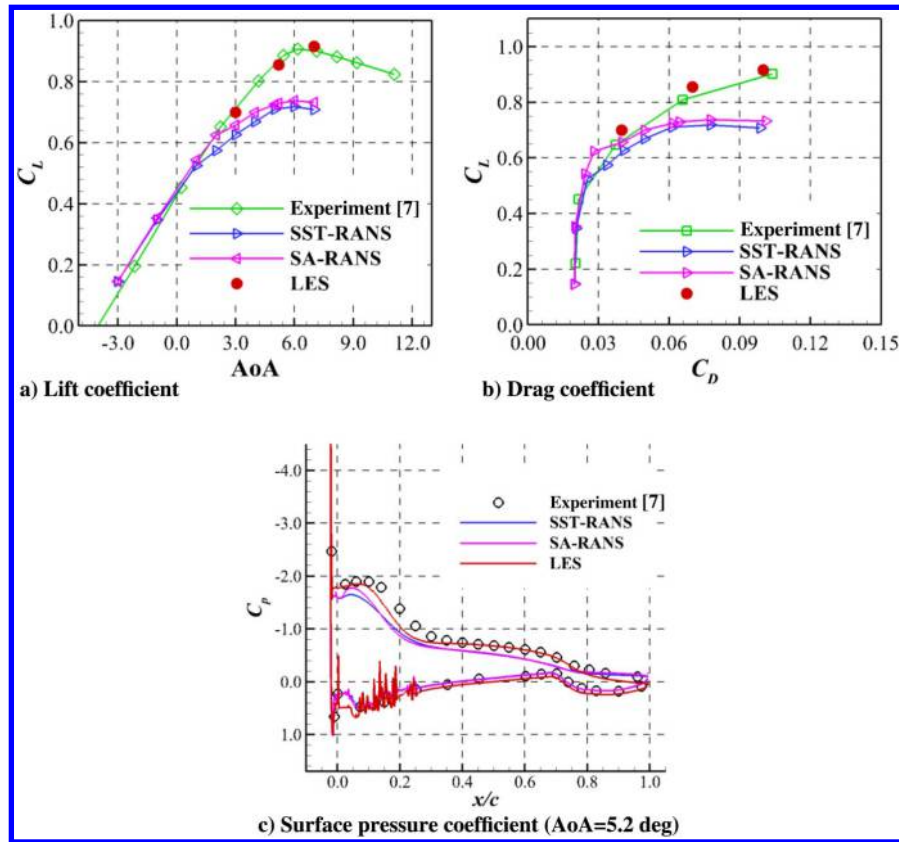


Fig. 6 Comparisons of computed mean force coefficients with experimental data for NLF-0414/623 iced airfoil ( $Ma = 0.21$ ,  $Re = 4.6 \times 10^6$ ).

using Spalart–Allmaras turbulence model [42] and Menter’s  $k - \omega$  shear stress transport (SST) turbulence model [43]. One can observe that both RANS models predict much lower lift and much higher drag near stall. In contrast, the LES predicts more accurately, with the relative errors of  $C_L$  and  $C_D$  less than 5 and 10%, respectively. Figure 6c further compares the mean surface pressure coefficients for  $AoA = 5.2$  deg. The pressure plateaus and then recovers progressively on the upper surface; this is correctly captured only by the LES.

The above results have exhibited the ability of the present LES in predicting aerodynamic forces and in reproducing turbulent unsteadiness, which gives credence to the idea of using the LES to compute the flow past an iced multi-element airfoil.

#### IV. Computational Configurations and Results

Figure 7 depicts the two ice shapes on the slat of the 30P30N airfoil. Although all three elements were accreted with ice in real

icing tests, only the ice on the slat is considered here because it causes dominant aerodynamic penalties [12]. Both ice accretions are 2D; there is no variation of shape or sweep angle in the spanwise direction. The ice heights are  $9\%c$  and  $8\%c$  for the streamwise ice and the horn ice, respectively. The computational freestream condition is  $Ma = 0.17$  and  $Re = 1.7 \times 10^6$ . For this condition, Figure 8 shows the curves of lift coefficient for the clean 30P30N airfoil obtained from the experiment at JAXA tunnel [40] and SST-RANS computation [43]. One can see that the RANS-computed lift coefficients agree well with the values from the experiment before  $AoA = 18$  deg. Based on the RANS data, stall occurs at approximately  $AoA = 20$  deg. In this study, the flows for  $AoA = 18, 20$ , and  $22$  deg are investigated. Under these  $AoAs$ , the flow has a separation bubble aft of the ice accretion, a typical feature of iced multi-element airfoil flow. The far-field boundary location, spanwise length, and boundary conditions are the same as those of the clean 30P30N validation case. The computational grid details and time

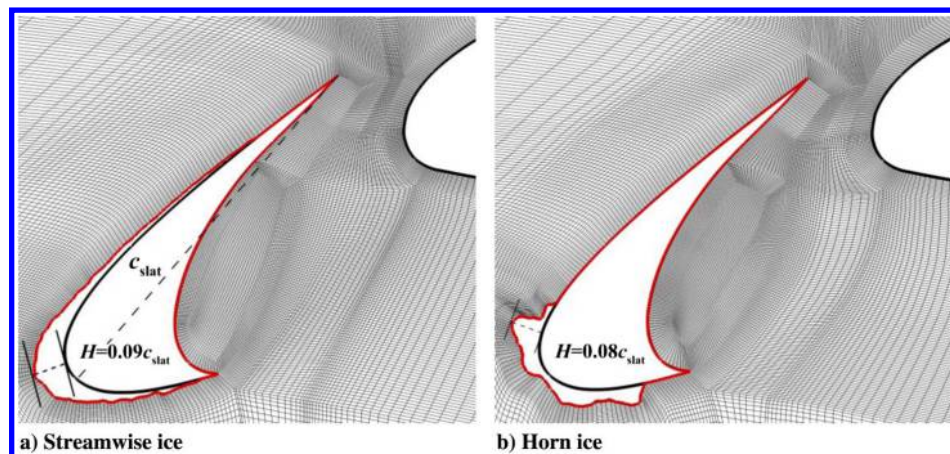


Fig. 7 Iced slat geometries along with grids.

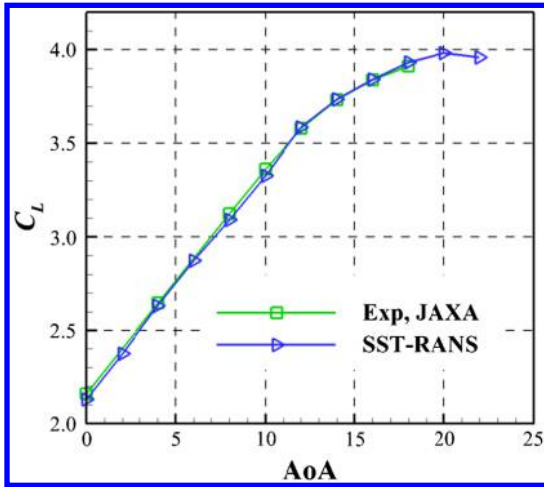


Fig. 8 Lift coefficients for the clean 30P30N airfoil obtained from experiment [40] and SST-RANS computation [43] ( $Ma = 0.17$ ,  $Re = 1.7 \times 10^6$ ).

steps are listed in Table 2. For the streamwise ice case, apart from a medium grid, a coarse grid is created by coarsening the cells of the medium grid by around 30% in each direction, and a fine grid is created by refining the cells of the medium grid by about 15% in each direction.

A precursor quasi-2D simulation is carried out first on a very coarse grid with only 20 cells along the span for each case. The fully developed flowfield is then interpolated to initialize the simulation on the computational grid listed in Table 2. Then approximately 25 time units ( $c/U_\infty$ ) are computed, and the final 10 time units are applied for statistical averaging. The computational times are approximately 0.43, 0.38, and 0.16 core hours per time step for the fine, medium, and coarse grids, respectively. The total computational cost is approximately 3.8 million core hours on an Intel Xeon 2.4 GHz cluster.

### A. Statistical Results

Figure 9 shows the time histories of  $C_L$  and  $C_D$  at  $AoA = 20^\circ$ . The mean values are listed in Table 3. Although both ice shapes slightly increase the slat lift, they dramatically decrease the lifts of the main element and the flap. The streamwise ice reduces the  $C_L$  values of the two elements by 15.41 and 9.50%, respectively, and the horn ice reduces them by 21.27 and 15.85%, respectively. In total, the two ice accretions decrease the airfoil lift by 10.66 and 16.45%, respectively. Moreover, the airfoil drag coefficient is increased by 40.58 and 59.42%, respectively. The two ice accretions increase the mean square root of the  $C_L$  fluctuations. For the streamwise ice case, Fig. 9 also shows the lift and drag histories obtained using both the coarse and fine grids; the corresponding time-averaged integral forces are listed in Table 4. One can observe that the results from different grids are very close although  $C_L$  decreases slightly and  $C_D$  increases a bit with grid refinement.

The ice-induced aerodynamic degradations can be reflected in the mean surface pressure coefficients (Fig. 10). The pressure exhibits a strong peak followed by pressure recovery on the slat upper surface for the clean case. In contrast, both ice accretions cause conspicuous pressure plateaus on the slat, and lower the suction peaks of the main element and the flap. The pressure coefficients on the slat cove surface are almost the same for the three cases, although the iced cases have a slightly lower pressure level. In addition, the ice accretions increase the slat chord, which partly accounts for the lift increase of the slat. For the streamwise ice case, Fig. 10 also shows the results obtained using the coarse and fine grids; both results almost coincide with that from the medium grid though the pressure on the slat upper surface increases a bit in the vicinity of the slat leading edge and decreases slightly near its trailing edge, as illustrated in Fig. 10.

Figure 11 shows the contours of the mean streamwise velocity around the slat and flap at  $AoA = 20^\circ$ . The flow is almost attached on the suction side of the clean slat except for a small laminar separation bubble. In contrast, it is fully separated for the iced slats; this aggravates the velocity defect in the slat wake, which in turn impedes the flow acceleration through the slat gap, lowers the suction peak of the main element, and even enlarges the flow separation above the flap. Obviously, the horn ice leads to severe

Table 2 Grid details and time steps for different configurations

Configuration	$N_{\text{total}}$ (million)	$N_{x,\text{slat}}$	$N_{x,\text{Main}}$	$N_{x,\text{flap}}$	$N_z$	First-layer height ( $\Delta y/c$ )	Time step ( $\Delta t U_\infty/c$ )
Clean	61.0	650	1050	500	100	$2.5 \times 10^{-4}$	$3.0 \times 10^{-5}$
Streamwise ice	62.1	680	1110	510	100	$2.5 \times 10^{-4}$	$3.0 \times 10^{-5}$
Horn ice	61.2	676	1092	498	100	$3.0 \times 10^{-4}$	$2.0 \times 10^{-5}$
Streamwise ice (coarse)	32.2	552	876	410	80	$2.5 \times 10^{-4}$	$3.0 \times 10^{-5}$
Streamwise ice (fine)	92.1	776	1272	580	116	$2.5 \times 10^{-4}$	$2.3 \times 10^{-5}$

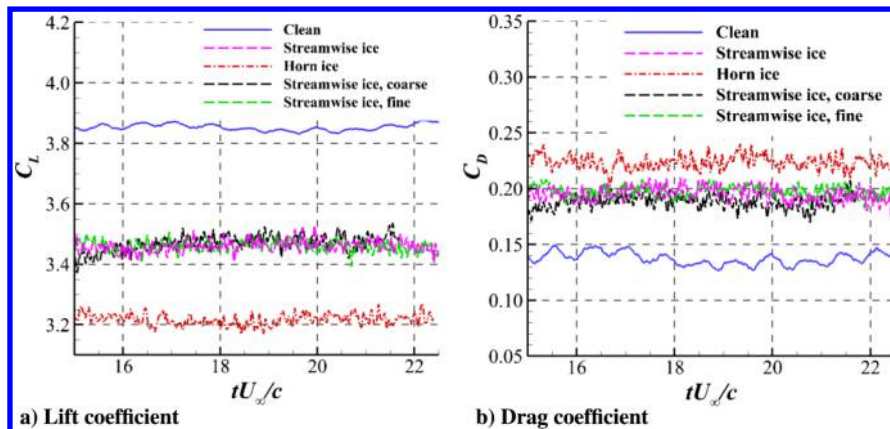


Fig. 9 Time histories of force coefficients ( $AoA = 20^\circ$ ).

**Table 3 Mean lift and drag coefficients of different configurations (AoA = 20 deg)**

Configuration	$C_L$	$C_{L,slat}$	$C_{L,Main}$	$C_{L,flap}$	$C_D$	$C_{D,p}$	$C_{D,f}$	$C_{L,rms}$	$C_{D,rms}$
Clean	3.854	0.702	2.868	0.284	0.138	0.026	0.0120	0.0116	0.0054
Streamwise ice	3.443	0.760	2.426	0.257	0.194	0.185	0.0085	0.016	0.0062
Horn ice	3.220	0.723	2.258	0.239	0.220	0.212	0.0081	0.018	0.0071

**Table 4 Mean lift and drag coefficients computed using three grids for the streamwise ice case (AoA = 20 deg)**

Force coefficients	Coarse grid	Medium grid	Fine grid
$C_L$	3.461	3.443	3.439
$C_D$	0.189	0.194	0.197

deterioration to the flowfield. In addition, the recirculation bubble in the slat cove is enlarged a bit due to ice accretion.

### B. Instantaneous Flowfields

Figure 12 shows the turbulent structures in the slat region for the clean case at AoA = 20 deg. The flow transitions to turbulence aft of a small laminar separation bubble, and the generated vortices become more 3D as they are transported downstream. In the slat cove, the flow is bounded by an SSL; the rollers forming in its initial region rapidly develop spanwise distortions that are amplified with downstream distance and finally break up into 3D structures. Near the impingement location of the slat cove, some vortices are reinjected into the recirculation region, and others escape through the gap after experiencing a streamwise elongation.

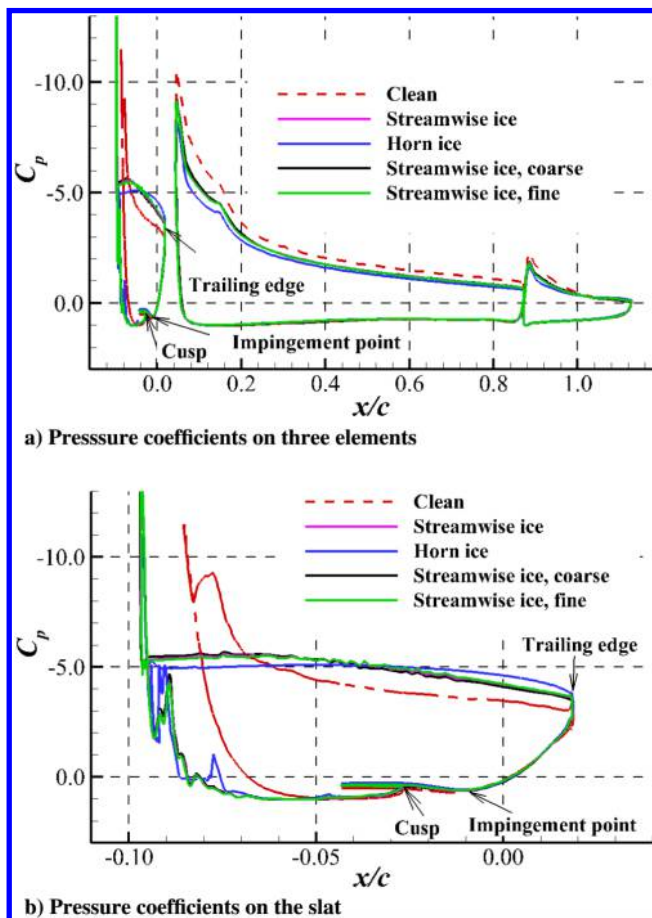
**Fig. 10 Comparison of mean surface pressure coefficients for different configurations (AoA = 20 deg).**

Figure 13 shows the eddy structures for the streamwise ice case at AoA = 20 deg. The ice accretion causes a complete change to the flow above the slat. The short laminar separation bubble in Fig. 12a bursts, yielding a completely separated flow over the slat upper surface. The ice-induced SSL shares many features with the SSL emanating from the slat cusp. Quasi-2D vortices appear and are deformed progressively into 3D structures such as hairpin vortices and streamwise vortices. Figure 14 further displays the instantaneous fields of spanwise vorticity for a clearer visualization. The vortices generated due to the K-H instability of the shear layers emanating from the ice tip, the slat cusp, and the trailing edge interact in the trailing-edge region and are advected downstream instead of impinging on the main element. The upper-surface recirculation region enlarges from 18 to 20 deg in the streamwise ice case, whereas it consistently occupies the entire surface in the horn ice case.

Figure 15 shows the eddy structures near the flap for the clean airfoil at AoA = 20 deg. The flow in the flap cove is similar to that in the slat cove. The SSL from the lip of the cove forms rollers and subsequent rib vortices in its initial region. In the impingement region, some vortices flow back into the recirculation region, and the remaining vortices escape through the flap gap. In the iced airfoil case, the flap cove vortices show a similar pattern as those of the clean airfoil, as shown in Fig. 16. However, many more low-speed vortices are convected over the main element from the slat wake, detrimental to the separation above the flap.

### C. Dominant Flow Unsteadiness

The above analysis shows that strong turbulent motions exist around an iced slat. Figure 17 shows the root mean square (rms) contours of the fluctuating pressure coefficient at AoA = 20 deg. The contours are left blank for values less than 0.05. For the clean airfoil, the pressure fluctuations are strong only near the leading-edge laminar separation bubble and along the slat cove SSL. In contrast, the fluctuations are greatly elevated for the iced airfoils due to the ice-induced energetic vortex motions. The fluctuations above the slat, in the slat cove, and in the initial trailing edge are all strengthened. Considering the similarity of the fluctuation patterns of both iced configurations, as displayed in Fig. 17, the following content only focuses on the fluctuations in the streamwise ice case.

Two-dimensional POD is implemented for the three subdomains demarcated in Fig. 18: the leading-edge region (LR), the trailing-edge region (TR), and the whole slat region (WR). In contrast to a full-domain POD, the subdomain POD shows strength by capturing more of a subdomain's total energy [44–46]. In addition, an FFT analysis is employed to obtain the spectra of turbulent fluctuations at the sampling points in Fig. 18. Points  $S_1$ – $S_7$  are in the ice-induced SSL; points  $L_1$ – $L_5$  are placed along the slat cove SSL; points  $M_1$ – $M_3$  are located in the slat wake;  $F_1$  is located in the near field. The pressure fluctuations at these points are sampled every 10 time steps. Five windows, with 50% overlap between adjacent windows and each with 16,384 sampling points, are used for FFT. The following aims to analyze the flow dynamics in the slat upper-surface SSL, in the slat cove SSL, and in the slat wake.

#### 1. Flow Dynamics in the Slat Upper-Surface SSL

Figure 19a shows the PSD of pressure fluctuations at points  $S_1$ – $S_3$ . Two strong peaks emerge from the broadband for  $S_2$  at 20 deg. The high-frequency peak is also conspicuous at  $S_1$ , and the low-frequency peak is also obvious at  $S_3$ . In addition, the spectrum of  $S_2$  at 22 deg also has two peaks. The high-frequency peak is the consequence of



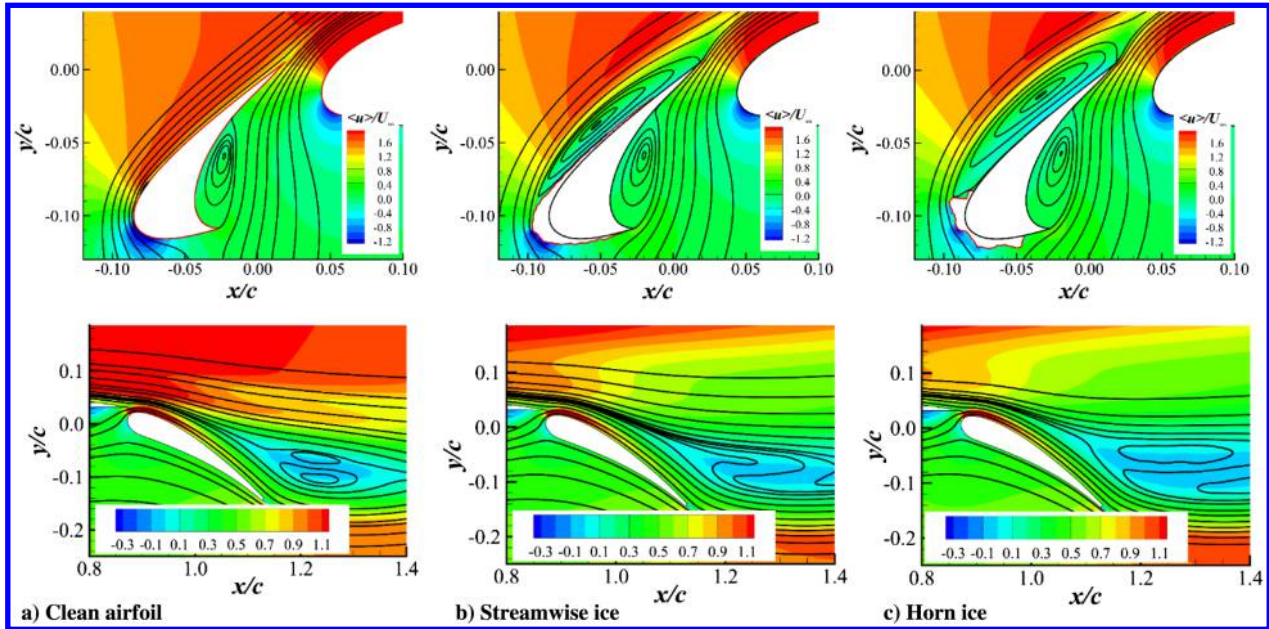


Fig. 11 Contours of the mean streamwise velocity  $\langle u \rangle/U_\infty$  ( $AoA = 20^\circ$ ).

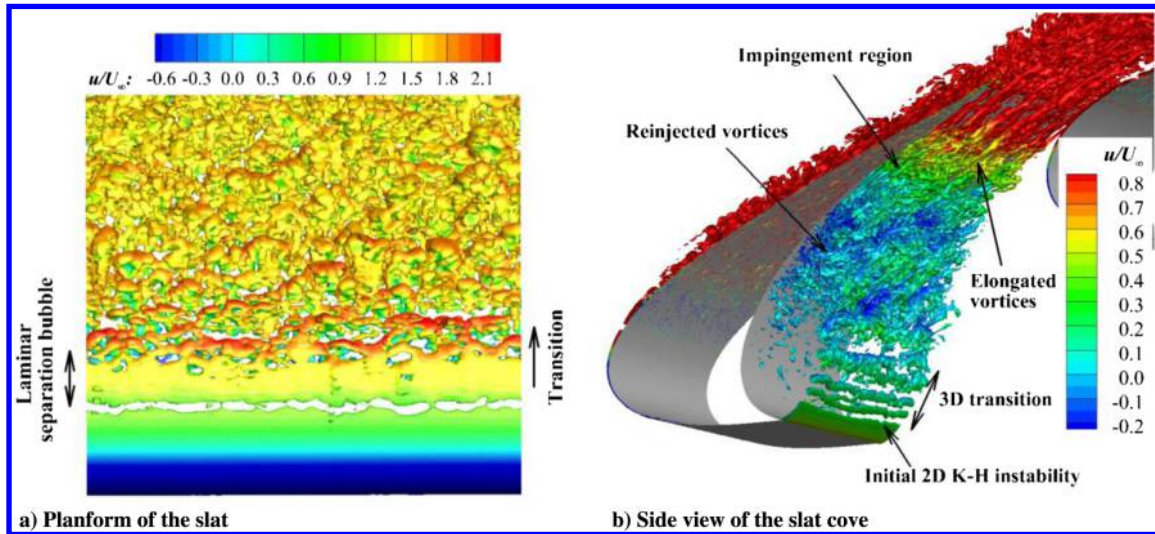


Fig. 12 Isosurfaces of  $Q(c/U_\infty)^2 = 5000$  colored by the streamwise velocity in the slat region of the clean airfoil ( $AoA = 20^\circ$ ).

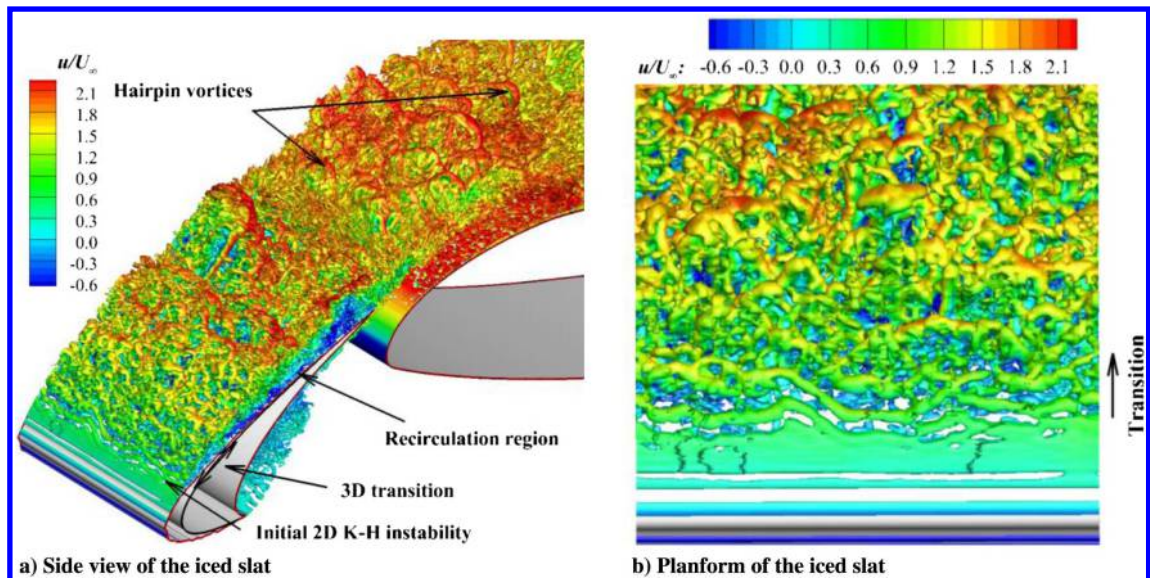


Fig. 13 Isosurfaces of  $Q(c/U_\infty)^2 = 5000$  colored by the streamwise velocity in the slat region for the streamwise ice case ( $AoA = 20^\circ$ ).



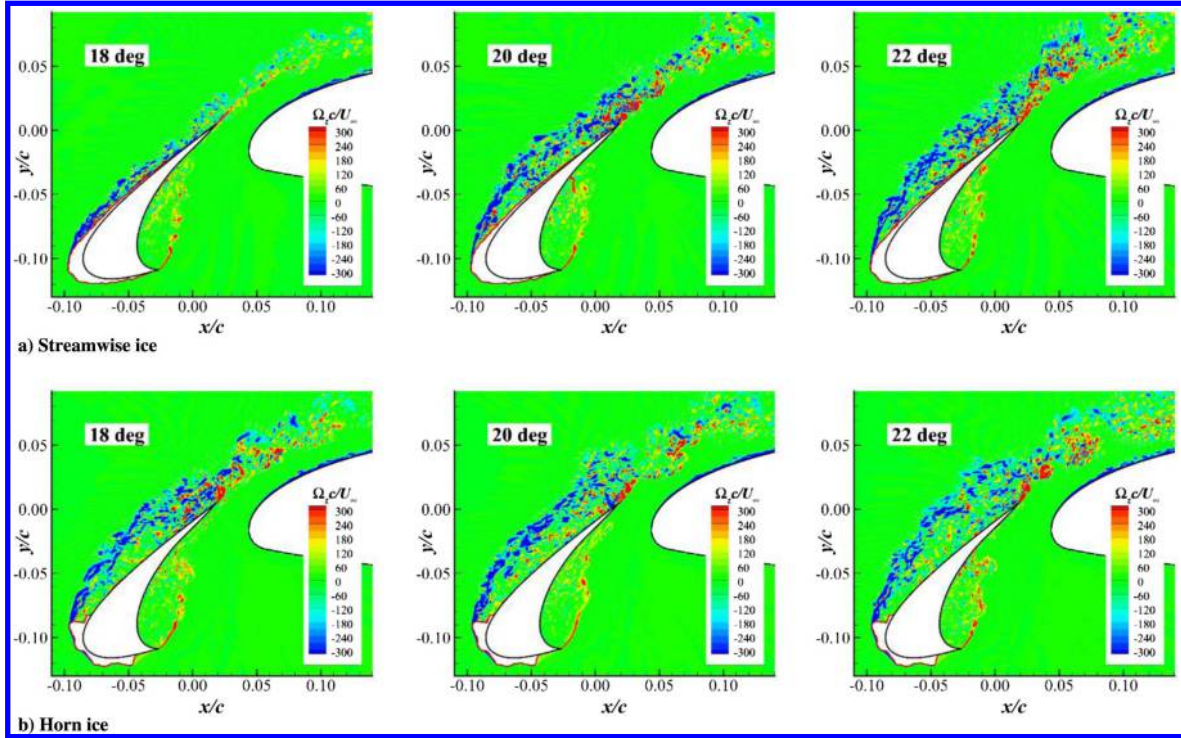


Fig. 14 Instantaneous spanwise vorticity  $\Omega_z c/U_\infty$  near the slat.

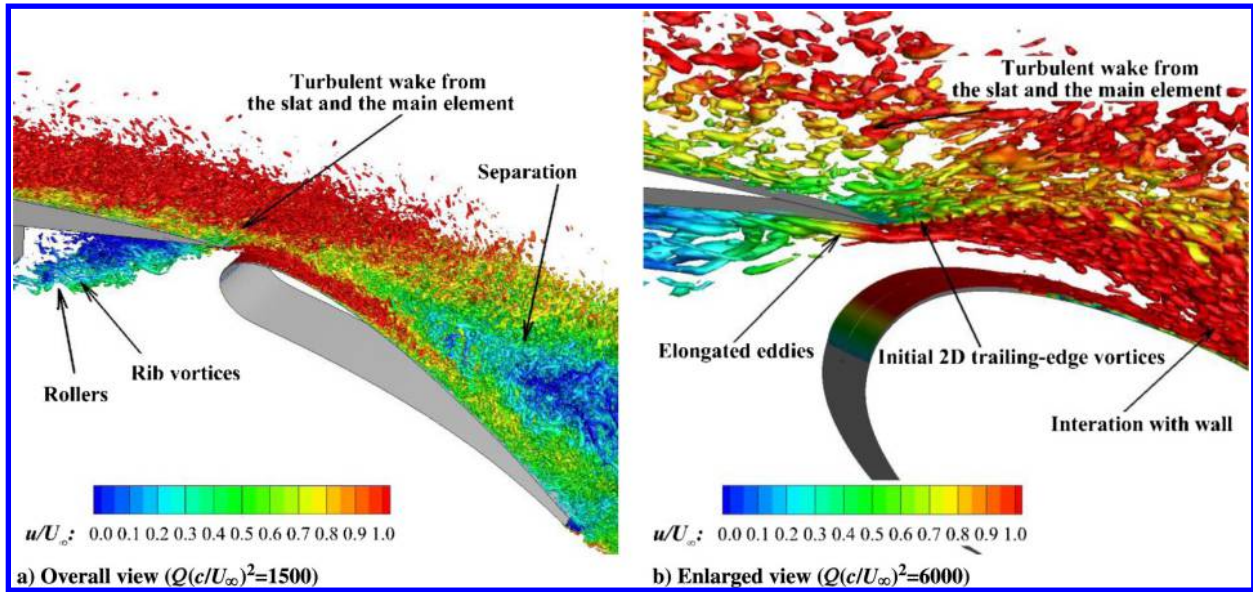


Fig. 15 Isosurfaces of  $Q$ -criteria colored by the streamwise velocity  $u/U_\infty$  in the flap region for the clean case (AoA = 20 deg).

the free-shear-layer K-H instability, and its nondimensional frequency is defined as [47]

$$St_\delta = \frac{f_1 \delta_w}{\bar{U}} \quad (9)$$

where  $\bar{U} = (U_{\text{high}} + U_{\text{low}})/2$  is the mean velocity across the shear layer, and  $\delta_w$  is the vorticity thickness defined by  $\delta_w = (U_{\text{high}} - U_{\text{low}})/\max(\partial U/\partial n)$ , where  $n$  denotes the shear-normal direction. Figure 19b shows the mean velocity profiles in the shear-normal direction at point  $S_1$ . Negative  $d/c_{\text{slat}}$  values denote the locations below  $S_1$ . One can obtain for AoA = 20 deg that  $U_{\text{high}}/U_\infty = 2.50$ ,  $U_{\text{low}}/U_\infty = -0.10$ , and  $\delta_w/c_{\text{slat}} = 7.3 \times 10^{-3}$ , yielding  $St_\delta = 0.176$ , which is slightly higher than the value 0.143

obtained from the linear stability analysis of a mixing shear layer [47]. This discrepancy should be expected because the current shear layer is not exactly identical to a canonical mixing layer due to the massive separation, the wall curvature effect, etc. Deck and Larauie [48] also reported certain nonconformity with the classic value.

The low-frequency peak  $f_2 c_{\text{slat}}/U_\infty = 14.5$ , half of the high-frequency  $f_1 c_{\text{slat}}/U_\infty = 29.0$ , is caused by vortex pairing. Figure 20 depicts the contours of instantaneous pressure coefficient fluctuations  $\Delta C_p = C_p - \langle C_p \rangle$  at three time moments with time intervals  $(t_2 - t_1)\bar{U}/\delta_w = 3.94$  and  $(t_3 - t_2)\bar{U}/\delta_w = 7.87$ , where  $\bar{U}/\delta_w$  is valued at point  $S_1$ . From  $t_1$  to  $t_3$ , vortex 1 and vortex 2 merge into one single vortex as they are advected downstream, which halves the vortex motion frequency. According to the study of a leading-edge separation bubble by Kitsios et al. [33], the vortex pairing is due to the

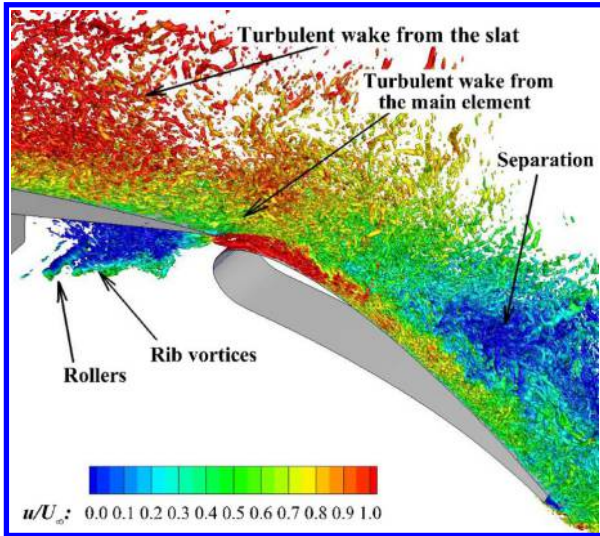


Fig. 16 Isosurfaces of  $Q(c/U_\infty)^2 = 1500$  colored by the streamwise velocity  $u/U_\infty$  in the flap region for the streamwise ice case (AoA = 20 deg).

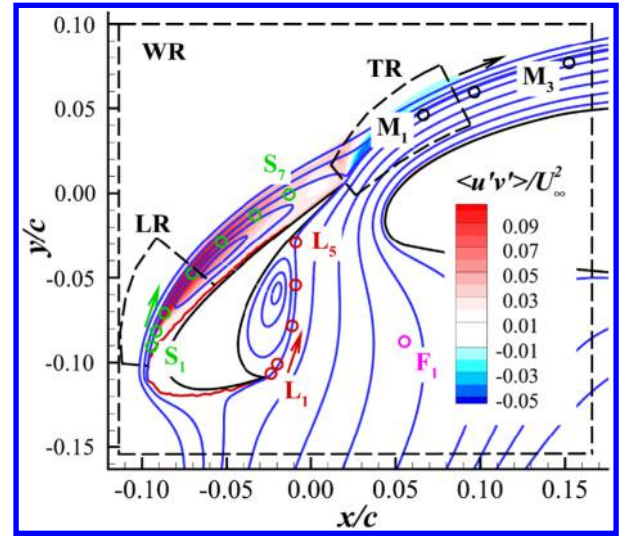


Fig. 18 Subdomains and probe locations for the streamwise ice case; the contour is the shear component  $\langle u'v' \rangle / U_\infty^2$  of the Reynolds stresses (AoA = 20 deg).

formation of lambda-shaped vortices at alternating spanwise locations from cycle to cycle, which results in a larger structure with twice the temporal period of the vortex roll-up due to K-H instability.

The vortex pattern can be more clearly demonstrated when we extract the dominant modes in the LR (Fig. 18) via POD. According to Simoni et al. [49], the shear-normal velocity component can better highlight the vortex shedding in contrast with the shear-parallel component. Therefore, the shear-normal velocity is applied here for POD. The snapshot details are shown in Table 5, where  $\Delta t_s U_\infty / c_{\text{slat}}$  is the time step between two snapshots and  $\Delta T_s U_\infty / c_{\text{slat}}$  is the total collection time. Figure 21 presents modes 4 and 9, which clearly highlight the regular vortex shedding. In contrast with mode 4, mode 9 captures finer structures, especially those in the initial SSL. The spectra of the POD temporal coefficients almost coincide for modes 8 and 9, both of which show a peak near the K-H instability frequency  $f_1 c_{\text{slat}} / U_\infty = 29.0$  (dashed red line). Likewise, the spectra for modes 3 and 4 are close, with a peak emerging around the frequency  $f_2 c_{\text{slat}} / U_\infty = 14.5$  (dashed blue line). The close agreement of the frequencies obtained by FFT and POD confirms the reliability of POD in identifying dominant structures as well as their motion frequencies. This motivates us to apply the analysis method to investigate more flow physics.

Figure 22a shows the first four POD spatial modes for the WR (Fig. 18). Here, the pressure coefficient is applied instead of the velocity component. It is difficult for a velocity-component-based POD in a 2D  $x$ - $y$  plane to obtain clear flow structures, because the velocity fluctuations in the spanwise direction can be comparable to

those in the other two directions, especially above the rear part of the slat. In Fig. 22a, all four modes exhibit regular structures along the slat upper surface. The first mode pair (modes 1 and 2) consists of low-frequency large-scale flow structures, and the second pair (modes 3 and 4) contains smaller ones. The modes in pair are characterized by a spatial shift of  $1/4$  wavelength, indicating a quasi-periodic motion of the flow structures. Figure 22b further displays modes 5–8. The identified structures break up into small irregular structures near the slat trailing edge, as revealed by mode 8; this is partly attributed to the interactions between the convected large-scale structures and the flow through the slat gap. In addition, modes 5 and 7 seem to exhibit complex structure interactions aft of  $x/c = -0.08$ .

## 2. Flow Dynamics in the Slat Cove SSL

Figure 23 shows the frequency spectra at points  $L_1$  and  $L_2$  (Fig. 18). A frequency peak at  $f_1 c_{\text{slat}} / U_\infty = 14.0$ , corresponding to K-H instability, is obvious for the streamwise ice case. At location  $L_1$ ,  $U_{\text{high}} / U_\infty = 0.73$ ,  $U_{\text{low}} / U_\infty = 0.10$ , and  $\delta_w / c_{\text{slat}} = 4.6 \times 10^{-3}$ , yielding  $St_\delta = 0.155$ , which agrees with the classic value of 0.143 [47]. In addition, several strong peaks emerge at nonharmonic discrete frequencies at locations  $L_1$ ,  $L_2$ , and  $F_1$ . Actually, these peaks become progressively salient from the impingement point toward the slat cusp along the SSL. These narrow bands are believed to be related to the acoustic resonance inside the slat cove. Terracol et al. [50], inspired by Rossiter [51], proposed a formula for predicting slat cove resonance frequencies:

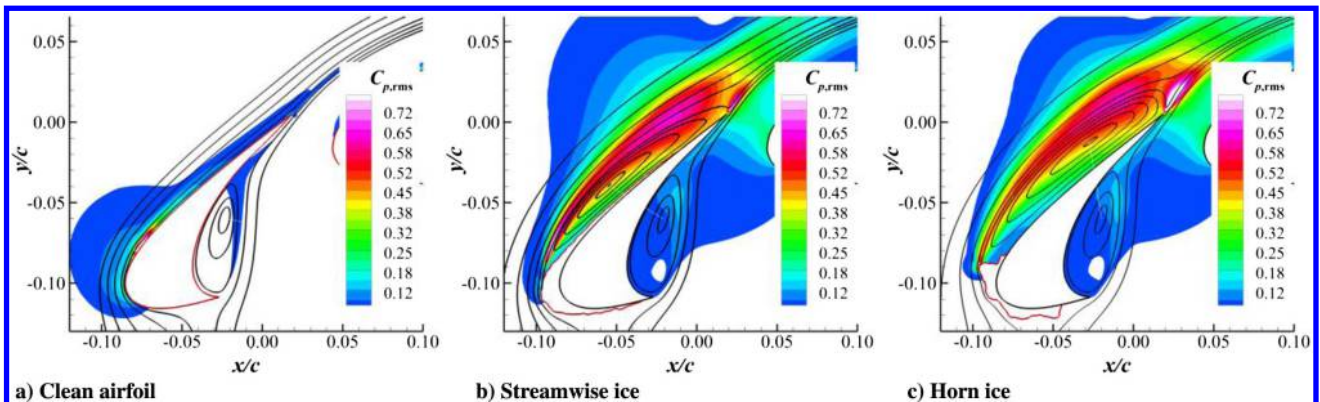


Fig. 17 RMS of the fluctuating pressure coefficient (AoA = 20 deg).



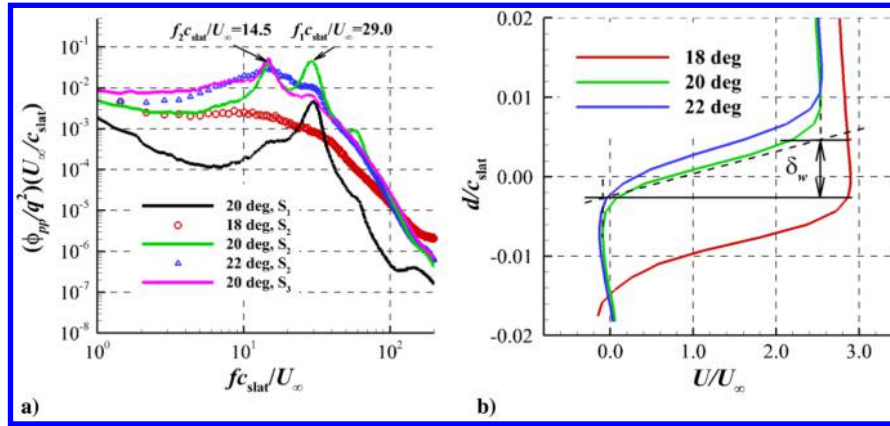


Fig. 19 a) PSD of pressure fluctuations at points  $S_1$ – $S_3$  and b) mean velocity profiles in the shear-normal direction at point  $S_1$  for the streamwise ice case.

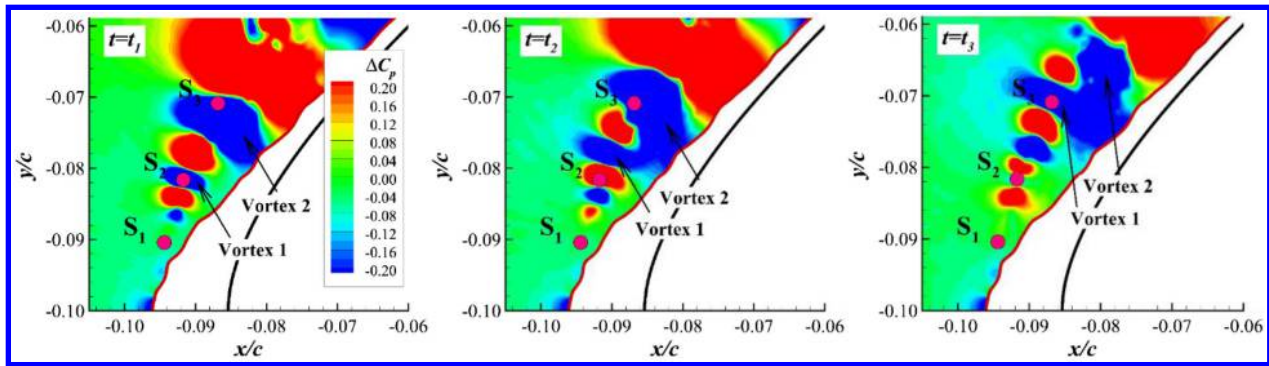


Fig. 20 Contours of instantaneous pressure coefficient fluctuations  $\Delta C_p = C_p - \langle C_p \rangle$  for the streamwise ice case ( $AoA = 20^\circ$  deg).

Table 5 Details of snapshots for POD

Subdomain	$N_{snap}$	$\Delta t_s U_\infty / c_{slat}$	$\Delta T_s U_\infty / c_{slat}$	Variable
LR	1024	0.002	2.048	Shear-normal velocity
WR	512	0.02	10.24	Pressure coefficient
TR	256	0.02	5.120	Shear-normal velocity

$$f_n = n \frac{U_\infty}{L_a} \frac{1}{M_\infty + \alpha_l / \kappa_v} \quad (10)$$

where  $L_a$  is the acoustic path, i.e., the straight-line distance between the slat cusp and the shear-layer impingement point;  $\alpha_l = L_v / L_a$  is the ratio of the mean SSL length  $L_v$  to the acoustic path  $L_a$ ; and  $\kappa_v = U_v / U_\infty$  characterizes the ratio of the mean convection velocity of vortices in the SSL to the freestream velocity. Here, the velocity  $U_v$  is approximated by the mean plateau velocity along the SSL [50]. Figure 24a gives the definitions of these flow-dependent quantities. In the present computation,  $L_a / c_{slat} = 0.544$ ,  $\alpha_l = 1.053$ , and  $\kappa_v = 0.524$ . Figure 24b compares the frequencies obtained from the present simulation and the model predictions for modes  $n = 1$ –3. In addition to the results predicted from the model of Terracol et al. [50], the results predicted by Heller and Bliss' model [52] and by Block's model [53] are also shown. The current LES results match well with all the model predictions.

Figure 24a also depicts the acoustic resonance mechanism inside the slat cove. The impingement of the SSL on the cove wall generates an acoustic wave that travels upstream. At the slat cusp, the shear layer responds to the pressure difference between the upstream acoustic wave outside the cove and the reflected downstream wave inside the cove by rolling up a vortex. The vortex travels downstream and impinges on the wall to generate sound and then initiate the feedback loop again. The resulting discrete acoustic resonance frequencies  $f_n$  can be interpreted as the vortical impingement frequencies. More explanations about the acoustic resonance in the slat cove can be found in [50].

Recalling Fig. 17, pressure fluctuations in the free shear layer emanating from the cusp are strongly elevated due to ice accretion. An inspection of a series of instantaneous pressure fields reveals that the elevation is obviously caused by the strong ice-induced pressure fluctuations (vortex motions) above the slat. Figure 25 shows the spectra of the temporal coefficients for the four most dominant POD

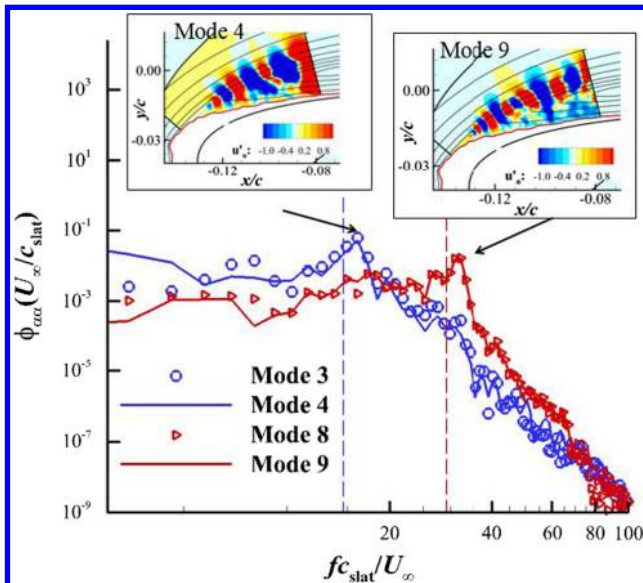


Fig. 21 PSD of the temporal coefficients in the LR for the streamwise ice case ( $AoA = 20^\circ$  deg); inserted contours are POD modes.



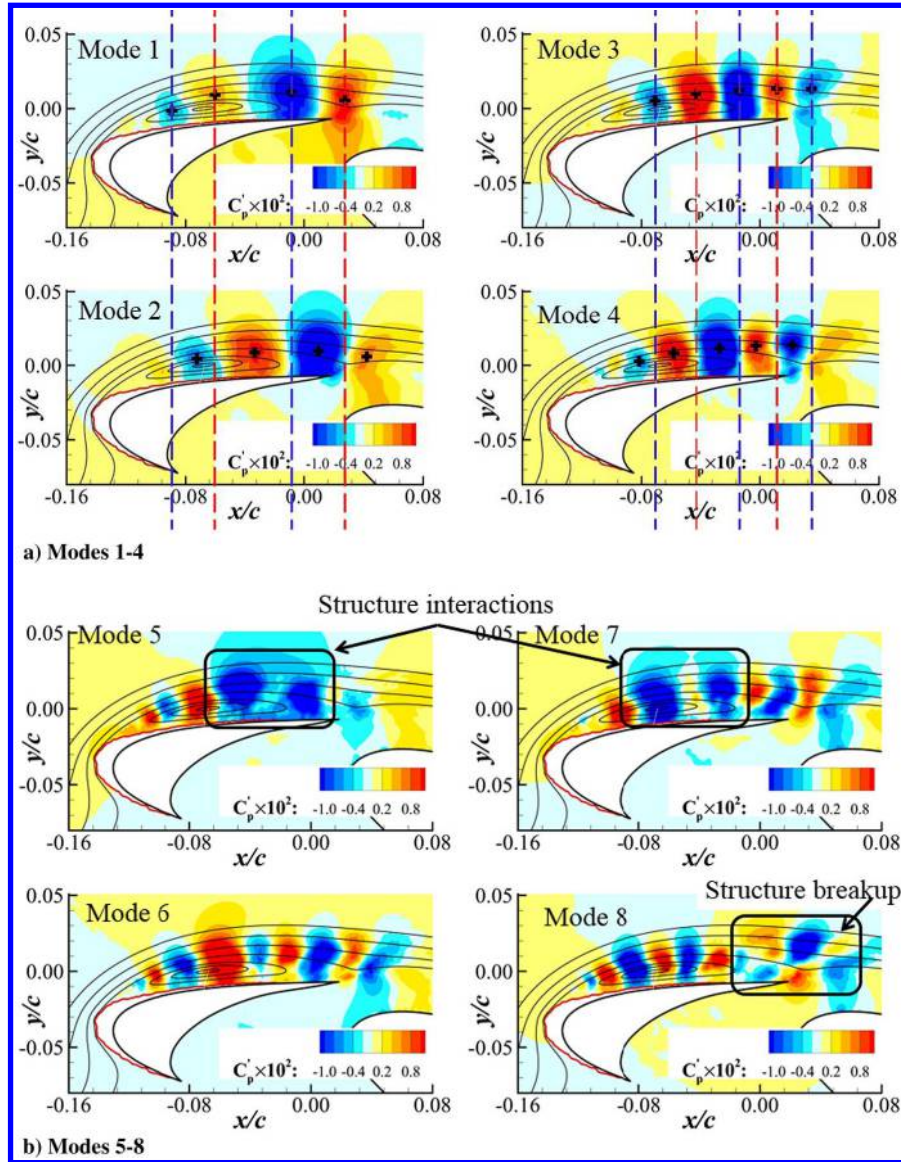


Fig. 22 POD modes of pressure coefficient in the WR for the streamwise ice case ( $\text{AoA} = 20^\circ$ ).

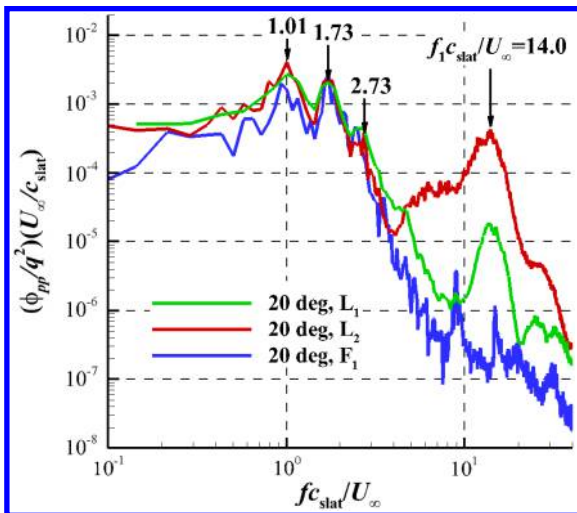


Fig. 23 PSD of pressure fluctuations at points  $L_1$ ,  $L_2$ , and  $F_1$  for the streamwise ice case ( $\text{AoA} = 20^\circ$ ).

modes displayed in Fig. 22a. The first mode pair (modes 1 and 2) captures the periodic motions of  $f c_{\text{slat}}/U_\infty = 1.01$  and  $1.83$ , and the second pair (modes 3 and 4) further identifies a periodic motion of  $f c_{\text{slat}}/U_\infty = 2.61$ . Interestingly, these three frequencies are almost equal to the three abovementioned acoustic resonance frequencies  $1.01$ ,  $1.73$ , and  $2.73$  in the slat cavity (denoted by dashed lines in Fig. 25), respectively. This implies that the vortex motion frequencies above the slat upper surface may be locked by the cavity acoustic resonance frequencies. This also means that the pressure fluctuations under the slat are intensified in particular at the three acoustic resonance frequencies. The arrows in Fig. 24a show the interactions between the vortex motions above the slat and the acoustic resonance inside the slat cavity.

### 3. Flow Dynamics in the Slat Wake

Compared with the LR, the flow in the TR is more chaotic due to the convection of the upstream turbulence, as shown in Fig. 13. Figure 26a shows the POD-identified spatial modes of the shear-normal velocity component and the PSD of their temporal coefficients. One can see that mode 5 exhibits regular vortex shedding. In fact, modes 5 and 6 are similar but are characterized by an approximately  $1/4$  spatial wavelength shift. Their spectra of temporal coefficients show a vortex shedding frequency around

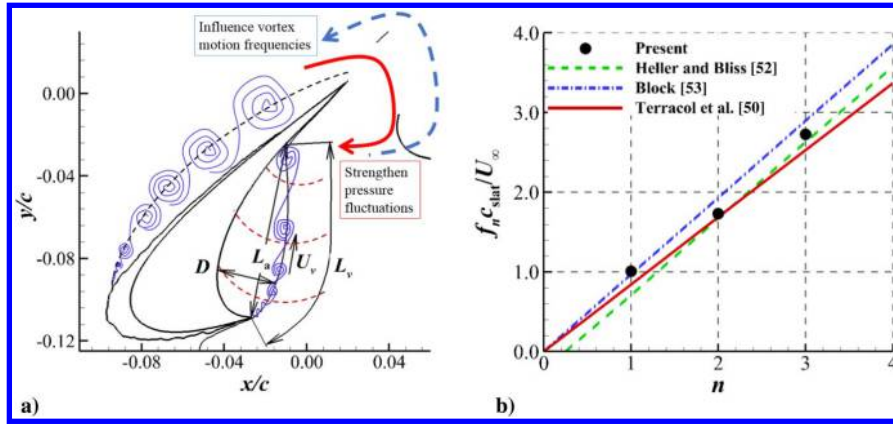


Fig. 24 a) Acoustic resonance in the slat cavity and b) comparison of the present LES-computed frequencies and those predicted by formulas for the streamwise ice case (AoA = 20 deg).

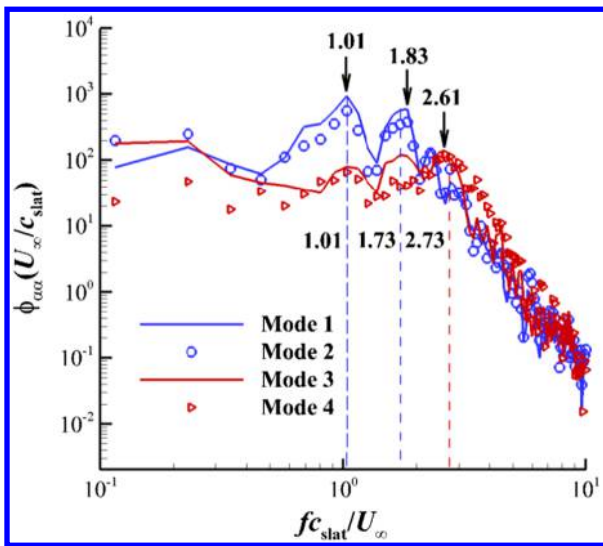


Fig. 25 PSD of the temporal coefficients in the WR for the streamwise ice case (AoA = 20 deg).

$f_1 c_{slat}/U_\infty = 8.5$ , which conforms to the fundamental frequency in the spectra of  $M_3$  (Fig. 26b) and is induced by K-H instability. Mode 1 shows a completely different pattern, with a higher energy rate (5.1%) than mode 5 (2.2%), because the large-scale structures from the upstream flow dominate the TR, as revealed in Fig. 22.

## V. Conclusions

Unsteady flow characteristics are investigated using the WMLES method with a low-dissipation hybrid central/upwind scheme for a 30P30N three-element airfoil with its slat accreted with streamwise ice and horn ice, respectively. The method is validated through an NLF-0414/623 iced airfoil and a clean 30P30N three-element airfoil.

Leading-edge ice accretions cause massive flow separation above the slat, which causes a pressure plateau on the slat suction side and a low-speed slat wake that impedes flow acceleration through the slat and flap gaps. This in turn leads to the unloading of the main element and the flap. In the present study, the streamwise ice and horn ice result in lift decreases of 10.66 and 16.45%, respectively, and drag increases of 40.58 and 59.42%, respectively.

The vortices above the iced slat first roll up from the leading-edge ice tip with a frequency of  $St_\delta = 0.176$ , which is slightly higher than the classic linear-stability-analysis value of 0.143 for a canonical mixing layer [47]. Then, the vortices pair with others, thereby halving the vortex motion frequency. The correct identification of both motions with their frequencies by POD demonstrates the validity of the analysis method. The vortices, developing downstream, comprise wide-ranging scales that dominate the entire slat upper surface. Then, they are convected over the main element and further deteriorate the flow over the flap.

In the iced slat cove, strong acoustic resonance is observed at the three discrete frequencies of  $f_n c_{slat}/U_\infty = 1.0$ – $3.0$ ,  $n = 1$ – $3$ , which agree well with the model predictions of Terracol et al. [50], Heller and Bliss [52], and Block [53]. The intensified resonance for the iced case results from the elevated pressure fluctuations along the cavity shear layer, which are in turn related to the propagation of

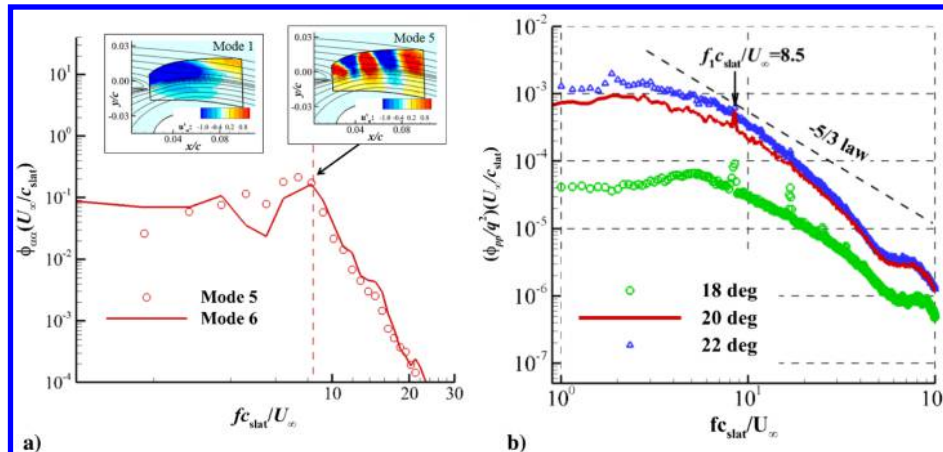


Fig. 26 a) PSD of the temporal coefficients in the TR (AoA = 20 deg) and b) PSD of the pressure fluctuations at point  $M_3$  for the streamwise ice case; inserted contours are modes 1 and 5.

the ice-induced pressure fluctuations from above the slat. The POD analysis reveals that the three most dominant ice-induced vortex motions above the slat occur near the three resonant frequencies, which implies that the ice-induced vortex motion frequencies might be locked by the cavity acoustic resonance frequencies. The flow downstream of the iced slat trailing edge is dominated by the large structures from upstream. Besides, the flow displays a frequency peak  $f_1 c_{\text{slat}}/U_\infty = 8.5$  with its several harmonics due to K-H instability.

### Acknowledgments

This work was supported by the National Natural Science Foundation of China (grant nos. 91852108 and 11872230) and Open Fund of Key Laboratory of Icing and Anti/De-icing (grant no. IADL20190201). The authors would like to express many thanks to the reviewers of this paper.

### References

- [1] Lynch, F. T., and Khodadoust, A., "Effects of Ice Accretions on Aircraft Aerodynamics," *Progress in Aerospace Sciences*, Vol. 37, No. 8, 2001, pp. 669–767.  
[https://doi.org/10.1016/S0376-0421\(01\)00018-5](https://doi.org/10.1016/S0376-0421(01)00018-5)
- [2] Pan, J., and Loth, E., "Detached Eddy Simulations for Iced Airfoils," *Journal of Aircraft*, Vol. 42, No. 6, 2005, pp. 1452–1461.  
<https://doi.org/10.2514/1.11860>
- [3] Bragg, M. B., Broeren, A. P., and Blumenthal, L. A., "Iced-Airfoil Aerodynamics," *Progress in Aerospace Sciences*, Vol. 41, No. 5, 2005, pp. 323–362.  
<https://doi.org/10.1016/j.paerosci.2005.07.001>
- [4] Addy, H., Broeren, A., Zoeckler, J., and Lee, S., "A Wind Tunnel Study of Icing Effects on a Business Jet Airfoil," NASA TM 2003-212124, 2003.
- [5] Broeren, A. P., Bragg, M. B., and Addy, H. E., "Flowfield Measurements About an Airfoil with Leading-Edge Ice Shapes," *Journal of Aircraft*, Vol. 43, No. 4, 2006, pp. 1226–1234.  
<https://doi.org/10.2514/1.19021>
- [6] Ansell, P. J., "Unsteady Modes in the Flowfield About an Airfoil with a Leading-Edge Horn-Ice Shape," Ph.D. Thesis, Univ. of Illinois at Urbana-Champaign, Urbana, IL, 2013.
- [7] Addy, H., and Chung, J., "A Wind Tunnel Study of Icing Effects on a Natural Laminar Flow Airfoil," *38th Aerospace Sciences Meeting and Exhibit*, AIAA Paper 2000-0095, 2000.  
<https://doi.org/10.2514/6.2000-95>
- [8] Ansell, P. J., and Bragg, M. B., "Characterization of Low-Frequency Oscillations in the Flowfield About an Iced Airfoil," *AIAA Journal*, Vol. 53, No. 3, 2015, pp. 629–637.  
<https://doi.org/10.2514/1.J053206>
- [9] Manshadi, M. D., and Esfeh, M. K., "Experimental Investigation of Flowfield over an Iced Aerofoil," *Aeronautical Journal*, Vol. 120, No. 1227, 2016, pp. 735–756.  
<https://doi.org/10.1017/aer.2016.29>
- [10] Ansell, P. J., and Bragg, M. B., "Unsteady Modes in Flowfield About Airfoil with Horn-Ice Shape," *Journal of Aircraft*, Vol. 53, No. 2, 2016, pp. 475–486.  
<https://doi.org/10.2514/1.C033421>
- [11] Ingelman-Sundberg, M., Trunov, O., and Ivaniko, A., "Methods for Prediction of the Influence of Ice on Aircraft Flying Characteristics," Rept. JR-1, a Joint Report from the Swedish-Soviet Working Group on Flight Safety, 1977.
- [12] Khodadoust, A., Dominik, C., Shin, J., and Miller, D., "Effect of In-Flight Ice Accretion on the Performance of a Multi-Element Airfoil," NASA TM 112174, 1995.
- [13] Potapczuk, M. G., and Berkowitz, B. M., "Experimental Investigation of Multielement Airfoil Ice Accretion and Resulting Performance Degradation," *Journal of Aircraft*, Vol. 27, No. 8, 1990, pp. 679–691.  
<https://doi.org/10.2514/3.25341>
- [14] Spalart, P. R., "Strategies for Turbulence Modelling and Simulations," *International Journal of Heat and Fluid Flow*, Vol. 21, No. 3, 2000, pp. 252–263.  
[https://doi.org/10.1016/S0142-727X\(00\)00007-2](https://doi.org/10.1016/S0142-727X(00)00007-2)
- [15] Chung, J., and Addy, H., "A Numerical Evaluation of Icing Effects on a Natural Laminar Flow Airfoil," *38th Aerospace Sciences Meeting & Exhibit*, AIAA Paper 2000-0096, 2000.  
<https://doi.org/10.2514/6.2000-96>
- [16] Pan, J., and Loth, E., "Reynolds-Averaged Navier–Stokes Simulations of Airfoils and Wings with Ice Shapes," *Journal of Aircraft*, Vol. 41, No. 4, 2004, pp. 879–891.  
<https://doi.org/10.2514/1.587>
- [17] Choo, Y. K., Thompson, D., and Mogili, P., "Detached-Eddy Simulations of Separated Flow Around Wings with Ice Accretions: Year One Report," NASA CR 2004-213379, 2004.
- [18] Alam, M. F., Thompson, D. S., and Walters, D. K., "Hybrid Reynolds-Averaged Navier–Stokes/Large-Eddy Simulation Models for Flow Around an Iced Wing," *Journal of Aircraft*, Vol. 52, No. 1, 2015, pp. 244–256.  
<https://doi.org/10.2514/1.C032678>
- [19] Xiao, M., Zhang, Y., and Chen, H., "Numerical Study of an Iced Airfoil Based on Delayed Detached Eddy Simulation with Low Dissipation Scheme," *9th AIAA Atmospheric and Space Environments Conference*, AIAA Paper 2017-3761, 2017.  
<https://doi.org/10.2514/6.2017-3761>
- [20] Zhang, Y., Habashi, W. G., and Khurram, R. A., "Zonal Detached-Eddy Simulation of Turbulent Unsteady Flow over Iced Airfoils," *Journal of Aircraft*, Vol. 53, No. 1, 2016, pp. 168–181.  
<https://doi.org/10.2514/1.C033253>
- [21] Costes, M., and Moens, F., "Advanced Numerical Prediction of Iced Airfoil Aerodynamics," *Aerospace Science and Technology*, Vol. 91, Aug. 2019, pp. 186–207.  
<https://doi.org/10.1016/j.ast.2019.05.010>
- [22] Xiao, M., Zhang, Y., and Zhou, F., "Numerical Study of Iced Airfoils with Horn Features Using Large-Eddy Simulation," *Journal of Aircraft*, Vol. 56, No. 1, 2019, pp. 94–107.  
<https://doi.org/10.2514/1.C034986>
- [23] Li, Z., Zhang, Y., and Chen, H., "A Low Dissipation Numerical Scheme for Implicit Large Eddy Simulation," *Computers & Fluids*, Vol. 117, Aug. 2015, pp. 233–246.  
<https://doi.org/10.1016/j.compfluid.2015.05.016>
- [24] Chen, H., Li, Z., and Zhang, Y., "U or V Shape: Dissipation Effects on Cylinder Flow Implicit Large-Eddy Simulation," *AIAA Journal*, Vol. 55, No. 2, 2017, pp. 459–473.  
<https://doi.org/10.2514/1.J055278>
- [25] Khalighi, Y., Ham, F., Nichols, J., Lele, S., and Moin, P., "Unstructured Large Eddy Simulation for Prediction of Noise Issued from Turbulent Jets in Various Configurations," *17th AIAA/CEAS Aeroacoustics Conference*, AIAA Paper 2011-2886, 2011.  
<https://doi.org/10.2514/6.2011-2886>
- [26] Roe, P. L., "Approximate Riemann Solvers, Parameter Vectors, and Difference Schemes," *Journal of Computational Physics*, Vol. 43, No. 2, 1981, pp. 357–372.  
[https://doi.org/10.1016/0021-9991\(81\)90128-5](https://doi.org/10.1016/0021-9991(81)90128-5)
- [27] Jiang, G. S., "Efficient Implementation of Weighted ENO Schemes," *Journal of Computational Physics*, Vol. 126, No. 1, 1996, pp. 202–228.  
<https://doi.org/10.1006/jcph.1996.0130>
- [28] Vreman, A. W., "An Eddy-Viscosity Subgrid-Scale Model for Turbulent Shear Flow: Algebraic Theory and Applications," *Physics of Fluids*, Vol. 16, No. 10, 2004, pp. 3670–3681.  
<https://doi.org/10.1063/1.1785131>
- [29] Kawai, S., and Larsson, J., "Wall-Modeling in Large Eddy Simulation: Length Scales, Grid Resolution, and Accuracy," *Physics of Fluids*, Vol. 24, No. 1, 2012, Paper 015105.  
<https://doi.org/10.1063/1.3678331>
- [30] Lumley, J. L., "The Structure of Inhomogeneous Turbulent Flows," *Atmospheric Turbulence and Radio Wave Propagation*, Vol. 790, edited by A. M. Yaglom, and V. I. Tatarski, Nauka, Moscow, 1967, pp. 166–178.
- [31] Fagley, C., Seidel, J., Siegel, S., and McLaughlin, T., "Reduced Order Modeling Using Proper Orthogonal Decomposition (POD) and Wavelet System Identification of a Free Shear Layer," *Active Flow Control II*, Springer, Berlin, 2010, pp. 325–329.
- [32] Mitchell, D. M., Honnery, D. R., and Soria, J., "Near-Field Structure of Underexpanded Elliptic Jets," *Experiments in Fluids*, Vol. 54, No. 7, 2013, p. 1578.  
<https://doi.org/10.1007/s00348-013-1578-3>
- [33] Kitsios, V., Cordier, L., Bonnet, J. P., Ooi, A., and Soria, J., "On the Coherent Structures and Stability Properties of a Leading-Edge Separated Aerofoil with Turbulent Recirculation," *Journal of Fluid Mechanics*, Vol. 683, Sept. 2011, pp. 395–416.  
<https://doi.org/10.1017/jfm.2011.285>
- [34] Cordier, L., and Bergmann, M., "Proper Orthogonal Decomposition: An Overview," *Lecture Series 2002-04, 2003-03 and 2008-01 Post-Processing of Experimental and Numerical Data*, Von Karman Inst. for Fluid Dynamics, Brussels, Belgium, 2008.
- [35] Choudhari, M., Khorrami, M., and Lockard, D., "Category 7 of BANC-II Workshop Slat Cove Noise: 30P30N 3-Element, Simplified High-Lift Configuration (Modified Slat)," 2012, [https://info.aiaa.org/tac/ASG/FDTC/DG/BECAN\\_files/\\_BANCII.htm](https://info.aiaa.org/tac/ASG/FDTC/DG/BECAN_files/_BANCII.htm) [retrieved 17 Nov. 2016].



- [36] Choudhari, M. M., and Lockard, D. P., "Assessment of Slat Noise Predictions for 30P30N High-Lift Configuration from BANC-III Workshop," *21st AIAA/CEAS Aeroacoustics Conference*, AIAA Paper 2015-2844, 2015.  
<https://doi.org/10.2514/6.2015-2844>
- [37] Addy, H., "Ice Accretions and Icing Effects for Modern Airfoils," NASA TP 2000-210031, 2000.
- [38] Pascioni, K., Cattafesta, L. N., and Choudhari, M. M., "An Experimental Investigation of the 30P30N Multi-Element High-Lift Airfoil," *20th AIAA/CEAS Aeroacoustics Conference*, AIAA Paper 2014-3062, 2014.  
<https://doi.org/10.2514/6.2014-3062>
- [39] Zhang, Y., Chen, H., Wang, K., and Wang, M., "Aeroacoustic Prediction of a Multi-Element Airfoil Using Wall-Modeled Large-Eddy Simulation," *AIAA Journal*, Vol. 55, No. 12, 2017, pp. 4219–4233.  
<https://doi.org/10.2514/1.J055853>
- [40] Murayama, M., Nakakita, K., Yamamoto, K., Ura, H., and Ito, Y., "Experimental Study of Slat Noise from 30P30N Three-Element High-Lift Airfoil in JAXA Hard-Wall Low-Speed Wind Tunnel," *20th AIAA/CEAS Aeroacoustics Conference*, AIAA Paper 2014-2080, 2014.  
<https://doi.org/10.2514/6.2014-2080>
- [41] Pascioni, K. A., and Cattafesta, L. N., "Aeroacoustic Measurements of Leading-Edge Slat Noise," *22nd AIAA/CEAS Aeroacoustics Conference*, AIAA Paper 2016-2960, 2016.  
<https://doi.org/10.2514/6.2016-2960>
- [42] Spalart, P., and Allmaras, S., "A One-Equation Turbulence Model for Aerodynamic Flows," *La Recherche Aerospaciale*, Vol. 1, No. 1, 1994, pp. 5–21.
- [43] Menter, F. R., "Two-Equation Eddy-Viscosity Turbulence Models for Engineering Applications," *AIAA Journal*, Vol. 32, No. 8, 1994, pp. 1598–1605.  
<https://doi.org/10.2514/3.12149>
- [44] Reichert, R. S., Hatay, F. F., Biringen, S., and Huser, A., "Proper Orthogonal Decomposition Applied to Turbulent Flow in a Square Duct," *Physics of Fluids*, Vol. 6, No. 9, 1994, pp. 3086–3092.  
<https://doi.org/10.1063/1.868133>
- [45] Moin, P., and Moser, R. D., "Characteristic-Eddy Decomposition of Turbulence in a Channel," *Journal of Fluid Mechanics*, Vol. 200, March 1989, pp. 471–509.  
<https://doi.org/10.1017/S0022112089000741>
- [46] Shah, M. K., and Tachie, M. F., "Proper Orthogonal Decomposition Analysis of Separated and Reattached Pressure Gradient Flows," *AIAA Journal*, Vol. 47, No. 11, 2009, pp. 2616–2631.  
<https://doi.org/10.2514/1.40095>
- [47] Huerre, P., and Monkewitz, P. A., "Local and Global Instabilities in Spatially Developing Flows," *Annual Review of Fluid Mechanics*, Vol. 22, No. 1, 1990, pp. 473–537.  
<https://doi.org/10.1146/annurev.fl.22.010190.002353>
- [48] Deck, S., and Laruffie, R., "Numerical Investigation of the Flow Dynamics Past a Three-Element Aerofoil," *Journal of Fluid Mechanics*, Vol. 732, Oct. 2013, pp. 401–444.  
<https://doi.org/10.1017/jfm.2013.363>
- [49] Simoni, D., Lengani, D., Ubaldi, M., Zunino, P., and Dellacasagrande, M., "Inspection of the Dynamic Properties of Laminar Separation Bubbles: Free-Stream Turbulence Intensity Effects for Different Reynolds Numbers," *Experiments in Fluids*, Vol. 58, No. 6, 2017, p. 66.  
<https://doi.org/10.1007/s00348-017-2353-7>
- [50] Terracol, M., Manoha, E., and Lemoine, B., "Investigation of the Unsteady Flow and Noise Generation in a Slat Cove," *AIAA Journal*, Vol. 54, No. 2, 2016, pp. 469–489.  
<https://doi.org/10.2514/1.J053479>
- [51] Rossiter, J. E., "Wind-Tunnel Experiments on the Flow over Rectangular Cavities at Subsonic and Transonic," Aeronautical Research Council Repts. & Memoranda No. 3438, London, 1964.
- [52] Heller, H., and Bliss, D., "The Physical Mechanism of Flow-Induced Pressure Fluctuations in Cavities and Concepts for Their Suppression," *2nd Aeroacoustics Conference*, AIAA Paper 1975-491, 1975.  
<https://doi.org/10.2514/6.1975-491>
- [53] Block, P. J. W., "Noise Response of Cavities of Varying Dimensions at Subsonic Speeds," NASA TN D-835, 1976.

C. Wen  
Associate Editor

**This article has been cited by:**

1. Yufei Zhang, Pu Yang, Runze Li, Haixin Chen. 2021. Unsteady Simulation of Transonic Buffet of a Supercritical Airfoil with Shock Control Bump. *Aerospace* **8**:8, 203. [[Crossref](#)]
2. Maochao Xiao, Yufei Zhang. 2021. Improved Prediction of Flow Around Airfoil Accreted with Horn or Ridge Ice. *AIAA Journal* **59**:6, 2318-2327. [[Citation](#)] [[Full Text](#)] [[PDF](#)] [[PDF Plus](#)]
3. Yuhui Yin, Pu Yang, Yufei Zhang, Haixin Chen, Song Fu. 2020. Feature selection and processing of turbulence modeling based on an artificial neural network. *Physics of Fluids* **32**:10, 105117. [[Crossref](#)]